Journal of
Materials Chemistry A

Materials for energy and sustainability

Accepted Manuscript

This article can be cited before page numbers have been issued, to do this please use: J. Liang, S. Ma, J. Li, Y. Wang, J. Wu, Q. Zhang, Z. Liu, Z. Yang, K. Qu and W. Cai, *J. Mater. Chem. A*, 2020, DOI: 10.1039/D0TA03622F.

ROYAL SOCIETY OF CHEMISTRY

rsc.li/materials-a

View Article Online
DOI: 10.1039/D0TA03622F

ARTICLE

Boosting the acidic electrocatalytic nitrogen reduction performance of MoS_2 by strain engineering

Received 00th January 20xx,
Accepted 00th January 20xx

DOI: 10.1039/x0xx00000x

Jiawei Liang,[a†] Shuangxiu Ma,[a†] Jing Li,[a] Yangang Wang,[c*] Junli Wu,[a] Quan Zhang,[a] Zhao Liu,[a] Zehui Yang,[a*] Konggang Qu[b] and Weiwei Cai[a*]

It is widely confirmed that expanding the layer spacing of layered-structural MoS_2 can boost the hydrogen evolution reaction (HER) activity of MoS_2. Inspired by this, strain engineering strategy is applied on defect-rich MoS_2 nanosheets by facilely F substitution to compress the interlayer space of MoS_2 owing to the smaller size and higher electronegativity of F than S and catalytic HER was remarkably surpressed. By considering the strongly reduced uphill energy for the hydrogenation of adsorbed N_2 on MoS_2 due to the introduction of F ions revealed by the first-principle calculation, electrochemical nitrogen reduction reaction (NRR) activity and selectivity on the F doped MoS_2 (F-MoS_2) catalyst in acidic condition can be significantly boosted. Faradic efficiency toward NRR on F-MoS_2 is therefore enhanced to 20.6% with the NH_3 yield high to 35.7 μg h^{-1} mg_{cat}^{-1} at the -0.2 V vs. RHE during the long-term operation.

Introduction

NH_3 is one of the most essential chemicals for the industrial producing of fertilizers, dyes and resins.[1, 2] Although both elements (N and H) in NH_3 are abundant on earth, the intrinsic inert property of N_2, which is the most abundant molecule in air, makes the producing of NH_3 from N_2 very difficult. Haber–Bosch process, which is the primary artificial NH_3 producing strategy nowadays, undergoes with metal catalyst under high temperatures (400–500 °C) and pressures (15–25 MPa). [3, 4] Around 1–2% of the world's energy supply is therefore consumed by the Haber–Bosch process. Energy-efficient strategies, represented by electrochemical nitrogen reduction reaction (NRR), were therefore widely studied.[5-10] Encouragingly, NRR using protons as hydrogen source can be efficiently powered by electricity under ambient condition. However, the most severe challenge for aqueous NRR is the poor efficiency ascribed to the competition between hydrogen evolution reaction (HER) and NRR.[11] HER is supposed to be one of the kinetically fastest electrochemical reactions due to that only two electrons are required to accomplish the reduction reaction and the standard redox potentials of H^+/H_2 ($E^0(H^+/H_2)$) and N_2/NH_3 ($E^0(N_2/NH_3)$) couples are very close. As a result, even using noble metals as catalyst, the activity and selectivity of NRR under ambient condition in aqueous electrolyte is much lower than expected due to the existence of competitive HER. [12] Actually, numerous noble-metal free catalysts have been developed for HER catalysis and highly efficient noble-metal-free hydrogen generation has been achieved.[13-15] Among which, MoS_2 has been considered as one of the most promising noble-metal-free HER catalysts due to the Pt-like property and proper Mo(III)/Mo(IV) redox potential (0.04 V)[16] and was also widely researched for NRR due to that requirements of NRR and HER on active sites are similar.[17-20] Density functional theory (DFT) calculations revealed that the edge of MoS_2 is the electrocatalytically active site for both NRR and HER [19] while the basal plane is inert for NRR. Great NRR activity in neutral condition was detected for MoS_2 with Faradic efficiency (FE) of 8.34% and NH_3 yield of 29.28 μg h^{-1} mg^{-1}_{cat} in 0.1 M Na_2SO_4. Unfortunately, NRR catalytic activity of MoS_2 in acidic condition, which is preferred for NRR due to that 6 H atoms are required for the fixation of every N_2 molecule [5, 20-24], is much poorer than the recently reported cost-effective NRR catalysts [25-29] ascribed to the great H^+ reduction activity of MoS_2. Strategies were applied to enhance the selectivity as well as NH_3 yield of MoS_2 based catalysts in acidic condition.[30-33] Ru/2H-MoS_2 interfaces were hence engineered with the acidic NRR FE enhanced to 17.6%. [31] Other than the noble-metal Ru, employing cost-effective active centers, including reduced graphene oxide [32] and single transition metal atom[33], can also boost the NRR activity and selectivity in acidic condition.

Here in this work, a facile strain engineering strategy was proposed to boost the acidic NRR activity and selectivity of defect-rich MoS_2 nano-sheets since strain engineering has been widely applied for electrocatalytic activity adjustment of both metallic [34-39] and transition metal complex catalysts [40-43]. Especially for the layered-structural MoS_2, interlayer space was expanded *via* different methods for HER catalytic activity improving.[44-46] Inspired by this, we proposed a facile strategy

[a] Sustainable Energy Laboratory, Faculty of Materials Science and Chemistry, China University of Geosciences Wuhan, 430074, China. willcai1985@gmail.com (W. Cai); yeungzehui@gmail.com (Z. Yang).
[b] Shandong Provincial Key Laboratory/Collaborative Innovation Center of Chemical Energy Storage & Novel Cell Technology, Liaocheng University, Liaocheng, 252059, China.
[c] College of Biological Chemical Science and Engineering, Jiaxing University, Jiaxing, Zhejiang, 314001, China. ygwang8136@mail.zjxu.edu.cn (Y. Wang)
† These authors contributed equally to this work.
Electronic Supplementary Information (ESI) available. See DOI: 10.1039/x0xx00000x

View Article Online
DOI: 10.1039/D0TA02622F

to compress the interlayer space of MoS_2 *via* F doping as demonstrated in **Scheme 1** to reduce the HER activity and therefore enhance the NRR selectivity by considering the small size of F ion and great electronegativity of F. Moreover, first-principle calculation reveals that the introduction of F ions would also significantly lower the uphill energy for the hydrogenation of adsorbed N_2, leading to the formation of highly active NRR catalytic centers. Due to the simultaneously enhanced NRR selectivity and activity, FE toward NRR of the F doped Mo_2S (F-Mo_2S) catalyst can be therefore strongly boosted 20.6% with the NH_3 yield high to 35.7 μg h^{-1} mg_{cat}^{-1} at -0.2 V vs. RHE.

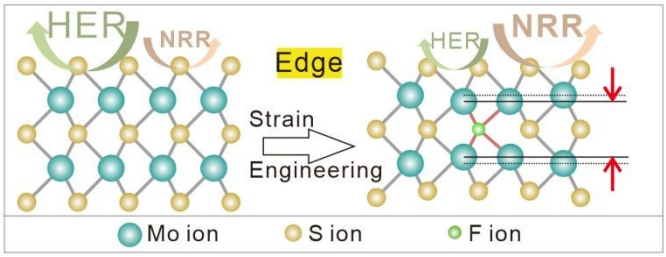

Scheme 1. Schematic diagram of strain engineering *via* F doping on the edge site of MoS_2 nanosheet.

Results and discussion

In order to confirm the successful synthesis of MoS_2 and the successful doping of F ions in F-MoS_2, X-ray diffraction (XRD) analysis was carried out (**Figure 1**a). All the diffraction peaks of F-MoS_2 agree well with the standard pattern of hexagonal MoS_2 (JCPDS card No. 73-1508), revealing the high purity of the product, while all the characteristic peaks of F-MoS_2 are negatively shifted as desired due to the smaller size and higher electronegativity of F than S. Especially, this negatively shifted (002) peak indicates that the layer spacing of the F-MoS_2 catalyst was slightly compressed since (002) facet is related to the interlayer of hexagonal MoS_2.[47, 48] Scanning electron microscope (SEM) image of the F-MoS_2 catalyst in Figure 1b reveals that the layered structure of the pristine MoS_2 (SEM image in Figure S1) was remained in F-Mo_2S. Meanwhile, the corresponding energy dispersive spectrum (EDS) reveals that atomic ratio of F in the F-MoS_2 catalyst is 1.12%, slightly higher than designed due to the better retention ability of F during the hyrothermal synthesis. By increasing the atomic ratio of S to F to 2:100 during the synthesis process, the F-MoS_2-2 sample was prepared. It can be found that the morphology of F-MoS_2-2 is remarkably changed compared with F-MoS_2 according to the SEM image of F-MoS_2-2 (Figure S2). The MoS_2 layers are accumulated for F-MoS_2-2 and the specific surface area would be strongly decreased due to the higher F content. Specific surface areas were therefore characterized using the Brumauer-Emmett-Teller (BET) method with N_2 adsorption-desorption isotherms displayed in Figure S3. The BET surface area of F-MoS_2-2 was decreased from 18 m^2/g of F-MoS_2 to 12 m^2/g as expected although more F ions would lead to extra defects. The observed wrinkled structure with crumpled edge and high transparency shown in both the transmission electron microscope (TEM) image (Figure S4) and the high-angle annular dark field scanning transmission electron microscope (HAADF-STEM) image of F-MoS_2 (Figure 1c) illustrates the ultrathin feature of the F doped MoS_2 nanoflakes of F-MoS_2. The corresponding EDS elemental mappings displayed in Figure 1d-f reveal that the F-MoS_2 catalyst is predominantly composed of Mo and S with F atoms doped uniformly.

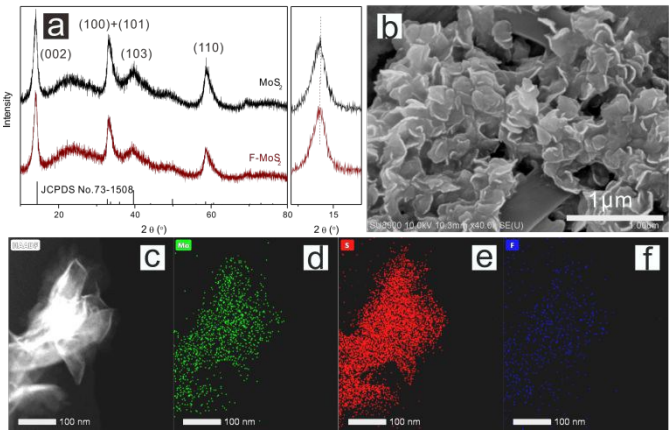

Figure 1. (a) XRD patterns of the pristine MoS_2 and F-MoS_2 catalysts; (b) SEM image, (c) HAADF-STEM image and (d-f) corresponding EDS elemental mapping images of the F-MoS_2 catalyst.

High-resolution transmission electron microscopy (HR-TEM) images are displayed in **Figure 2** to in-detail reveal the micro-morphology and strain effect of the F-MoS_2 flake. It can be detected from the HR-TEM images on edge of the F-MoS_2 flakes (Figure 2a-b) that the F-MoS_2 flakes mainly consist of 3-6 S-Mo-S layers with numerous defects engineered. By measuring the thickness of a typical 5-layer nanosheet in Figure 2b, distance of a single S-Mo-S layer can be calculated to be 0.58 nm, which is decreased by 8% compared with the pristine defect-rich MoS_2 nanosheet prepared from the same strategy [48]. For the purpose of further confirming the effect of F doping on compression of the MoS_2 interlayer distance, Raman analysis was carried out on both F-MoS_2 and pristine MoS_2 (Figure S5). Note that both the E^1_{2g} and A_{1g} bands of the F-MoS_2 Raman spectrum shift to a lower wavenumber compared with the pristine MoS_2, indicating that layered-structural MoS_2 sheets were compressed by the doped F ions [49, 50]. HR-TEM image on F-MoS_2 surface (Figure 2c) shows that defects are exsited. Note that numerous crystal fringes are discontinuous in Figure 2c, indicating the existence of 1T/2H phase interfaces, which is further manifested by the selected area electron diffraction (SAED) pattern (insert of Figure 2c) in the form of six independent diffraction arcs, a representative quasiperiodic structure with rich defects.

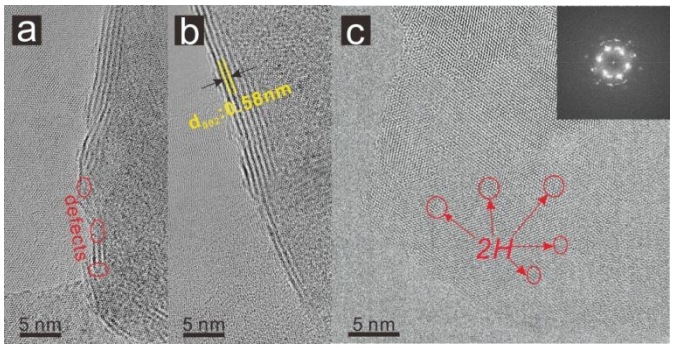

Figure 2. HR-TEM images on (a-b) edge and (c) surface of the F-MoS_2 catalyst.

Sub-angstrom resolution HAADF-STEM image on surface of the F–MoS_2 were taken to clearly identify the defects and phase interfaces of the F-MoS_2 catalyst (**Figure 3**a). A trigonal lattice structure corresponding to the 1T–MoS_2 and the common honeycomb lattice area of the 2H–MoS_2 are both clearly visible with interphase lined. At the same time, the uniformly dark regions as marked in red circles confirm the existence of defects on the F-MoS_2 surface. As a supplementary evidence for the extra surface defects, which are not as effective on electrochemical catalysis as the edge defects, formed by F doping. The F-MoS_2 catalyst possesses higher BET surface area (18 m^2/g) compared with the pristine MoS_2 (10 m^2/g) due to the remained edge defects and additionally generated surface defects. X-ray photoelectron spectroscopy (XPS) analysis was subsequently executed to in detail study the elemental composition and surface chemical state of the F-MoS_2 catalyst. The survey XPS spectrum of the F-MoS_2 catalyst (Figure S6) confirms the existence of F in the F-MoS_2 catalyst and the F content in the F-MoS2 is 1.04 atom.%, very close to the SEM-EDS result. The Mo 3d high resolution XPS spectrum of the F-MoS_2 catalyst (Figure 3b) reveals a doublet of predominantly characteristic 1T phase peaks of Mo $3d_{3/2}$ and Mo $3d_{5/2}$ located at 231.4 eV and 228.2 eV, which are much lower than that of their 2H phase counterparts (232.1 eV and 229.0 eV). Negatively shifted S 2p peak (Figure S7) can confirm the transfer of MoS_2 from 2H to 1T phase in the F-MoS_2 catalyst. Interestingly, further quantitative analysis based on the deconvoluted Mo 3d resonances exhibited that content of 1T phase in the F-MoS_2 catalyst is increased compared with the pristine MoS_2 although the interlayer distance was compressed.

Although the additional defects and the enhanced 1T phase content in F-MoS_2 should be benificial for HER catalysis in common sence, HER activity of MoS_2 was strongly suppressed by the doped F ions due to the strain effect according to the linear sweep voltammogramm (LSV) curves (Figure 3c). The HER current density at -0.3 V vs. RHE was strongly decreased by 43.5% for the F-MoS_2 catalyst compared with the pristine MoS_2 atalyst. It can be therefore indicated that HER activity of surface defects as well as phase interfaces of MoS_2 is much lower than that of the edge-defects. In the case of F-MoS_2, activity of edge-defects was strongly reduced due to the compression effect of F ions. As a result, it is reasonable to imply that F-MoS_2 may possess greater acidic NRR selectivity.

With the saturated gas in electrolyte changed to N_2, acidic LSV of both MoS_2 and F-MoS_2 are positively shifted compared with those collected in Ar-saturated electrolyte due to the widely approved NRR activity of MoS_2 (Figure S8). Especially at 1 mA/cm^2, overpotential of MoS_2 was decreased by 11 mV, attributed to reduction of N_2, while this value is increased to 23 mV for the F-MoS_2 catalyst. This significant difference between the LSV curves of F-MoS_2 in Ar and N_2 condition indicates the great selectivity of F-MoS_2 on NRR. Similary, LSV current density difference of F-MoS_2-2 with higher F content measured in Ar and N_2 condition is also remarkable (Figure S9) although the activity in both Ar and N_2 conditions was decayed due to the reduction of defects. By directly comparing the LSV curves of the two catalysts collected in N_2 saturated 0.05 M H_2SO_4 solution (Figure 3d), current density decrement at -0.3 V vs. RHE ascribed to F doping is significantly reduced to 28.4%, ca. half of that in Ar saturated electrolyte. More importantly, current density of F-MoS_2 is high to 2.36 mA/cm^2, which is even 22.6% higher than that of the pristine MoS_2 catalyst at -0.25 V vs. RHE. The strongly changed electrochemical catalytic property caused by the ambient adjustment can confirm the great selectivity of active sites in F-MoS_2 toward NRR.

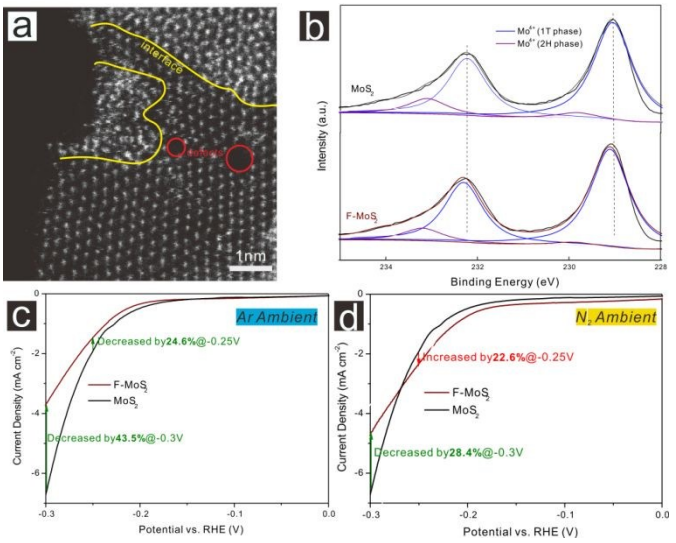

Figure 3. (a) Sub-angstrom resolution HAADF-STEM image on surface of the F–MoS_2 flake. (b) Mo 3d high resolution XPS spectra and the pristine MoS_2 and F-MoS_2 catalysts. LSV curves of MoS_2 and F-MoS_2 measured in (c) Ar and (d) N_2 saturated 0.05 M H_2SO_4 solutions.

Since great NRR selectivity of F-Mo_2S in acidic condition was experimentally confirmed, first-principle calculation was subsquently deployed to theoretically evaluate the effect of F doping on the catalytic NRR activity of MoS_2. The distal pathway in the association mechanism is more feasible than other pathways since it allows stabilizing the intermediates:

***+N_2(g)→*N_2→*NNH→*NNH_2→*N+NH_3(g)→*NH→*NH_2→*NH_3→*+ NH_3(g)**

Mo sites on the edge of MoS_2 layers were chosen as the primary active sites of the NRR process since the Mo atom has both empty d orbitals which can accept the long-pair electrons

from N_2 molecules and the occupied d orbitals which are capable of reducing the N_2 triple bond significantly. The free energy changes and the structures of each step of both MoS_2 and F-MoS_2 in NRR process are displayed in **Figure 4**. It can be noted that free energy change of nitrogen adsorption on F-MoS_2 edge (-0.85 eV) is significantly lower than MoS_2 (-0.38 eV), which suggested that the introduction of F atom can enhance the N_2 absorption ability on F-MoS_2. The Gibbs free energy diagram for MoS_2 (Figure 4a) showed that the first hydrogenation step of the adsorbed N_2 molecule occurs difficultly with an uphill free energy change of 0.64 eV. For the subsequent elementary reaction steps of the distal mechanism, the hydrogenation of *N-NH_2 was followed by the release of first NH_3 and then the *N intermediate was formed. It can be therefore considered that the formation of *N-NH, which bears the highest uphill free energy of 0.64 eV, is the rate-determining step of NRR on MoS_2. For F-MoS_2, the Gibbs free energy change of the same rate-determining step is only 0.36 eV, which is 44% lower than that of MoS_2 (Figure 4b), aggreeing well with the significantly reduced NRR onset potential of F-MoS_2 comapred with the pristine MoS_2.

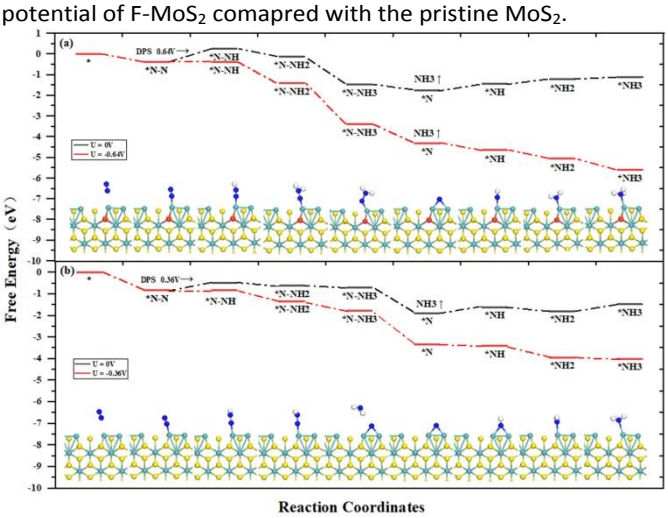

Figure 4. Gibbs free energy diagrams of distal pathways for NRR on (a) F-MoS_2 and (b) F-MoS_2 at different applied potentials. (White, yellow, red, cyan and blue balls represent the H, S, F, Mo and N atoms, respectively.)

Since the effect of F doping on promotion of NRR selectivity and activity of F-MoS_2 are confirmed, chronoamperometry (CA) measurements were therefore carried out in N_2 saturated 0.05 M H_2SO_4 electrolyte (Figure S10) to quantitatively analyze the NRR performance of F-MoS_2 by utilizing the traditional indophenol blue method [51]. Typical double-cell three-electrode electrochemical setup with catalyst coated glassy carbon electrode as working electrode were used for the CA measurements and the calibration curves are displayed in Figure S11. UV-vis absorption spectra of the electrolyte stained with indophenol indicator after 2 h electrolysis at a series of potentials for MoS_2 and F-MoS_2 are displayed in Figure S12. It is suggested that both MoS_2 and F-MoS_2 can catalyze NRR at -0.15 V vs. RHE and potentials ranging from -0.30 V to -0.15 V vs. RHE are selected to study the NRR electrocatalysis performance.

NH_3 yield calculated from the partial current densities for NH_3 production at various applied potential on MoS_2 and F-MoS_2 are compared in **Figure 5**a. Although overall current densities on these two catalysts are increased with the applied potential during the CA test (Figure S10), NH_3 yield is undependent on the applied potential. By considering the catalyst loading on the electrode, average NH_3 yield at -0.20 V vs. RHE of the F-MoS_2 catalyst is high to 35.7 μg h^{-1} mg_{cat}^{-1}, which is among the best reported cost-effective NRR catalysts (Table S1). At the same time, this value is also higher than those measured at -0.15 V and -0.25 V vs. RHE. In contrast, NH_3 yield catalyzed by MoS_2 at -0.2 V vs. RHE is ca. 50% lower compared with that catalyzed by F-MoS_2 as desired although NH_3 yield of MoS_2 at -0.15 V vs. RHE is much higher than that of F-MoS_2. As another important descriptor of NRR performance, FE of the catalysts was calculated (detail in Supporting Information) to evaluate the selectivity of NRR catalysts (Figure 5b). As expected, NRR FE of the F-MoS_2 catalyst is much greater than that of the pristine MoS_2 catalyst at applied potentials ranging from -0.20 V to -0.30 V vs. RHE. Especially at -0.2 V vs. RHE, NRR FE of the F-MoS_2 catalyst can reach 20.6%, which is among those of the best reported noble-metal-free catalysts (Table S1) and is also much greater than that of the pristine MoS_2. In order to confirm the superior NRR catalytic activity of F-MoS_2, we also carried out the Nuclear Magnetic Resonance (NMR) tests to quantitatively analyze the ammonia concentration from the established standard curve (Figure S13).[52] An intensive $^{14}NH_4^+$ NMR signal was detected for F-Mo_2S and the calculated Faradaic efficiency and NH_3 yield rate was similar to the UV-vis method shown in Figure 5c. Also, only $^{15}NH_4^+$ signal was recorded with $^{15}N_2$ as feeding gas depicting that and the N_2 gas, other than the residual contaminants from the catalyst synthesis, was the nitrogen source for the formation of NH_3. Durability of NRR on F-MoS_2 was subsequently investigated by repeatedly performing the CA tests with NH_3 yield (Figure 5d) and NRR FE (Figure S14) collected. Both great activity and selectivity can be retained during the durability test. NH_3 yield is higher than 30 μg h^{-1} mg_{cat}^{-1} and FE is higher than 20% for all the five repeated tests. After 10 h continuously testing, NRR FE of NH_3 production on the F-MoS_2 catalyst is calculated to be 26%, which is even higher than that of the first two hours.

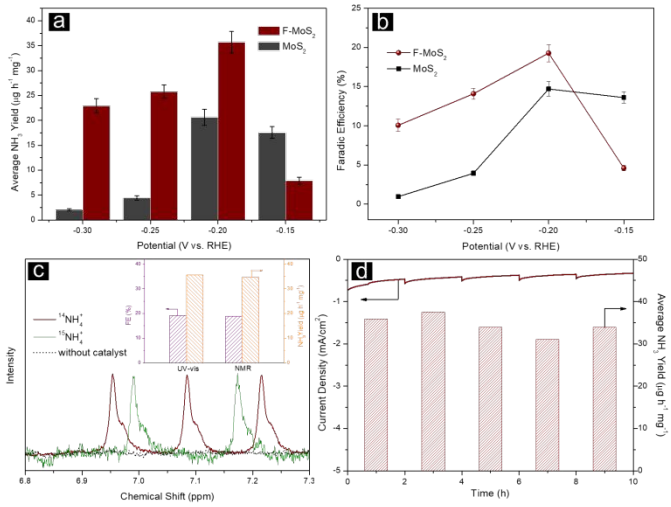

Figure 5. (a) Average yield rate of NH_3 production and (b) NRR FE at different applied potentials on MoS_2 and F-MoS_2; (c) NMR spectra of electrolyte after NRR catalysis by F-MoS_2 (insert: comparison of Faradaic efficiency and NH_3 yield rate of F-MoS_2 between UV-vis and NMR methods); (d) 10 h durability test for F-MoS_2 toward N_2 electrochemical reduction at -0.2 V vs. RHE.

Methods

Catalyst synthesis. The F-MoS_2 catalyst was prepared by a conventional hydrothermal method [45, 48]. 2.2836 g sulfocarbamide as S source and 11.1 mg NH_4F as F source (atomic ratio of S to F is set to be 100:1) were dissolved in 40 mL deionized water under stirring for 30 min. Subsequently, 0.2358 g ammonium molybdate was added to form a homogeneous solution. The mixed solution was then transferred into a 50 mL Teflon-lined stainless steel autoclave and kept at 220 °C for 18 h. After cooled to room temperature, the product was washed with deionized water and ethanol for three times to remove any residual reactants. Same procedures were used for the pristine MoS_2 preparation without NH_4F.

First-principle calculation. The calculations were performed with the Vienna Ab-initio Simulation Package (VASP). [53-55] The Perdew-Burke-Ernzerhof (PBE) approximation [56] of density functional theory (DFT) was used to describe the exchange-correlation interactions and the projector augmented wave (PAW) method [57] to account for core-valence interactions. The energy cutoff for plane wave expansions was set to 400 eV, and the reciprocal space was sampled by a 2×2×1 grid which is generated by VASPKIT [58]. At least 15 Å vacuum layer was applied in the z-direction of the slab models to prevent the vertical interactions between slabs. All structures were fully relaxed to the ground state and spin-polarization was considered in all calculations. The convergence thresholds for structural optimization was set at 0.02 eV/Å in force and the convergence criterion for energy is 1×10^{-5} eV.

The reaction Gibbs free energy changes (ΔG) for each step were based on the computational hydrogen electrode model proposed by Nørskov *et al* [59, 60], and can be calculated using the following equation:

$$\Delta G = \Delta E + \Delta ZPE - T\Delta S + \Delta G_U + \Delta G_{pH}$$

where ΔE is obtained directly from DFT calculations, ΔZPE is the change in zero-point energies (ZPE), T is the temperature (298.15 K), and ΔS is the change in entropy of products and reactants.

Details on material characterizations, electrochemical measurements and quantification of ammonia are provided in Supporting Information.

Conclusions

In summary, F ions were employed into the lattice of layered-structural MoS_2 to compress the interlayer space to simultaneously improve the NRR selectivity and activity in acidic condition. HER activity of the F-MoS_2 catalyst is strongly reduced due to the strain effect and the NRR selectivity of the F-MoS_2 catalyst is therefore strongly enhanced. Since NRR activity of Mo_2S can also be significantly boosted by the doped F ions according to the first-principle calculation, F-Mo_2S was therefore considered as a superior NRR catalyst with relatively low cost. At relatively low overpotential (-0.2 V vs. RHE), NH_3 yield resulted from NRR is high to 35.7 μg h^{-1} mg_{cat}^{-1} with a great NRR FE of 20.6%. By considering the great durability of F-MoS_2, this work provides a facile strategy for the destination of efficient N_2 fixation catalysts.

Conflicts of interest

There are no conflicts to declare.

Acknowledgements

We are grateful for financial support from the National Natural Science Foundation of China (Nos. 21875224, 21703211 and 21703212).

Notes and references

1. Z. Geng, Y. Liu, X. Kong, P. Li, K. Li, Z. Liu, J. Du, M. Shu, R. Si and J. Zeng, *Adv. Mater.*, 2018, **30**, 1803498.
2. C. Lv, C. Yan, G. Chen, Y. Ding, J. Sun, Y. Zhou and G. Yu, *Angew. Chem. Int. Ed.*, 2018, **57**, 6073-6076.
3. C. J. M. van der Ham, M. T. M. Koper and D. G. H. Hetterscheid, *Chem. Soc. Rev.*, 2014, **43**, 5183-5191.
4. P. C. Dos Santos, R. Y. Igarashi, H.-I. Lee, B. M. Hoffman, L. C. Seefeldt and D. R. Dean, *Acc. Chem. Res.*, 2005, **38**, 208-214.
5. Q. Wang, Y. Lei, D. Wang and Y. Li, *Energy Environ. Sci.*, 2019, **12**, 1730-1750.
6. S. Zhao, X. Lu, L. Wang, J. Gale and R. Amal, *Adv. Mater.*, 2019, **31**, 1805367.
7. A. J. Martin, T. Shinagawa and J. Perez-Ramirez, *Chem*, 2019, **5**, 263-283.
8. X. Guo, H. Du, F. Qu and J. Li, *J. Mater. Chem. A*, 2019, **7**, 3531-3543.
9. K.-H. Liu, H.-X. Zhong, S.-J. Li, Y.-X. Duan, M.-M. Shi, X.-B. Zhang, J.-M. Yan and Q. Jiang, *Prog. Mater Sci.*, 2018, **92**, 64-111.
10. S. L. Foster, S. I. P. Bakovic, R. D. Duda, S. Maheshwari, R. D. Milton, S. D. Minteer, M. J. Janik, J. N. Renner and L. F. Greenlee, *Nat. Catal.*, 2018, **1**, 490-500.

11. K. A. Brown, D. F. Harris, M. B. Wilker, A. Rasmussen, N. Khadka, H. Hamby, S. Keable, G. Dukovic, J. W. Peters, L. C. Seefeldt and P. W. King, *Science*, 2016, **352**, 448-450.
12. R. Manjunatha and A. Schechter, *Electrochem. Commun.*, 2018, **90**, 96-100.
13. J. Xiong, J. Li, J. Shi, X. Zhang, N.-T. Suen, Z. Liu, Y. Huang, G. Xu, W. Cai, X. Lei, L. Feng, Z. Yang, L. Huang and H. Cheng, *ACS Energy Lett.*, 2018, **3**, 341–348.
14. Y. Zheng, Y. Jiao, A. Vasileff and S.-Z. Qiao, *Angew. Chem. Int. Ed.*, 2018, **57**, 7568-7579.
15. X. X. Zou and Y. Zhang, *Chem. Soc. Rev.*, 2015, **44**, 5148-5180.
16. Z. Luo, Y. Ouyang, H. Zhang, M. Xiao, J. Ge, Z. Jiang, J. Wang, D. Tang, X. Cao, C. Liu and W. Xing, *Nat. Commun.*, 2018, **9**, 2120.
17. K. H. Liu, H. X. Zhong, S. J. Li, Y. X. Duan, M. M. Shi, X. B. Zhang, J. M. Yan and Q. Jiang, *Prog. Mater Sci.*, 2018, **92**, 64-111.
18. B. H. R. Surrnto, D. B. Wang, L. M. Azofra, M. Harb, L. Cavallo, R. Jalili, D. R. G. Mitchell, M. Chatti and D. R. MacFarlane, *ACS Energy Lett.*, 2019, **4**, 430-435.
19. L. Zhang, X. Q. Ji, X. Ren, Y. J. Ma, X. F. Shi, Z. Q. Tian, A. M. Asiri, L. Chen, B. Tang and X. P. Sun, *Adv. Mater.*, 2018, **30**, 1800191.
20. X. Li, T. Li, Y. Ma, Q. Wei, W. Qiu, H. Guo, X. Shi, P. Zhang, A. M. Asiri, L. Chen, B. Tang and X. Sun, *Adv. Energy Mater.*, 2018, **8**, 1801357.
21. L. Han, X. Liu, J. Chen, R. Lin, H. Liu, F. Lu, S. Bak, Z. Liang, S. Zhao, E. Stavitski, J. Luo, R. R. Adzic and H. L. Xin, *Angew. Chem. Int. Ed.*, 2019, **58**, 2321-2325.
22. Z. Geng, Y. Liu, X. Kong, P. Li, K. Li, Z. Liu, J. Du, M. Shu, R. Si and J. Zeng, *Adv Mater*, 2018, DOI: 10.1002/adma.201803498, e1803498.
23. W. Qiu, X. Y. Xie, J. Qiu, W. H. Fang, R. Liang, X. Ren, X. Ji, G. Cui, A. M. Asiri, G. Cui, B. Tang and X. Sun, *Nat. Commun.*, 2018, **9**, 3485.
24. J. Han, X. Ji, X. Ren, G. Cui, L. Li, F. Xie, H. Wang, B. Li and X. Sun, *J. Mater. Chem. A*, 2018, **6**, 12974-12977.
25. W. H. Zhao, L. F. Zhang, Q. Q. Luo, Z. P. Hu, W. H. Zhang, S. Smith and J. L. Yang, *ACS Catal.*, 2019, **9**, 3419-3425.
26. L. Q. Li, C. Tang, B. Q. Xia, H. Y. Jin, Y. Zheng and S. Z. Qiao, *ACS Catal.*, 2019, **9**, 2902-2908.
27. H. Y. Chen, X. J. Zhu, H. Huang, H. B. Wang, T. Wang, R. B. Zhao, H. G. Zheng, A. M. Asiri, Y. L. Luo and X. P. Sun, *Chem. Commun.*, 2019, **55**, 3152-3155.
28. Y. Wang, X. Q. Cui, J. X. Zhao, G. R. Jia, L. Gu, Q. H. Zhang, L. K. Meng, Z. Shi, L. R. Zheng, C. Y. Wang, Z. W. Zhang and W. T. Zheng, *ACS Catal.*, 2019, **9**, 336-344.
29. X. Ren, J. X. Zhao, Q. Wei, Y. J. Ma, H. R. Guo, Q. Liu, Y. Wang, G. W. Cui, A. M. Asiri, B. H. Li, B. Tang and X. P. Sun, *ACS Central Sci.*, 2019, **5**, 116-121.
30. L. M. Azofra, C. Sun, L. Cavallo and D. R. MacFarlane, *Chem. Eur. J.*, 2017, **23**, 8275-8279.
31. B. H. R. Suryanto, D. Wang, L. M. Azofra, M. Harb, L. Cavallo, R. Jalili, D. R. G. Mitchell, M. Chatti and D. R. MacFarlane, *ACS Energy Lett.*, 2019, **4**, 430-435.
32. X. Li, X. Ren, X. Liu, J. Zhao, X. Sun, Y. Zhang, X. Kuang, T. Yan, Q. Wei and D. Wu, *J. Mater. Chem. A*, 2019, **7**, 2524-2528.
33. J. Zhao, J. Zhao and Q. Cai, *PCCP*, 2018, **20**, 9248-9255.
34. M. Luo and S. Guo, *Nat. Rev. Mater.*, 2017, **2**, 17059.
35. L. Gan, R. Yu, J. Luo, Z. Cheng and J. Zhu, *J. Phys. Chem. Lett.*, 2012, **3**, 934-938.
36. L. Gan, M. Heggen, S. Rudi and P. Strasser, *Nano Lett.*, 2012, **12**, 5423-5430.
37. M. Escudero-Escribano, A. Verdaguer-Casadevall, P. Malacrida, U. Gronbjerg, B. P. Knudsen, A. K. Jepsen, J. Rossmeisl, I. E. L. Stephens and I. Chorkendorff, *J. Am. Chem. Soc.*, 2012, **134**, 16476-16479.
38. M. Du, L. Cui, Y. Cao and A. J. Bard, *J. Am. Chem. Soc.*, 2015, **137**, 7397-7403.
39. L. Bu, N. Zhang, S. Guo, X. Zhang, J. Li, J. Yao, T. Wu, G. Lu, J.-Y. Ma, D. Su and X. Huang, *Science*, 2016, **354**, 1410-1414.
40. A. Castellanos-Gomez, R. Roldan, E. Cappelluti, M. Buscema, F. Guinea, H. S. J. van der Zant and G. A. Steele, *Nano Lett.*, 2013, **13**, 5361-5366.
41. S. Bertolazzi, J. Brivio and A. Kis, *ACS Nano*, 2011, **5**, 9703-9709.
42. D. Y. Hwang, K. H. Choi, J. E. Park and D. H. Suh, *PCCP*, 2017, **19**, 18356-18365.
43. K. Liang, Y. Yan, L. Guo, K. Marcus, Z. Li, L. Zhou, Y. Li, R. Ye, N. Orlovskaya, Y.-H. Sohn and Y. Yang, *ACS Energy Lett.*, 2017, **2**, 1315-1320.
44. J. Xiong, J. Li, J. Shi, X. Zhang, W. Cai, Z. Yang and H. Cheng, *Appl. Catal., B*, 2019, **243**, 614-620.
45. W. Cai, X. Luo, Y. Jiang, Z. Liu, J. Li, L. Ma, J. Xiong, Z. Yang and H. Cheng, *Int. J. Hydrogen Energy*, 2018, **43**, 2026-2033.
46. K. Sun, L. Zeng, S. Liu, L. Zhao, H. Zhu, J. Zhao, Z. Liu, D. Cao, Y. Hou, Y. Liu, Y. Pan and C. Liu, *Nano Energy*, 2019, **58**, 862-869.
47. Y.-J. Tang, Y. Wang, X.-L. Wang, S.-L. Li, W. Huang, L.-Z. Dong, C.-H. Liu, Y.-F. Li and Y.-Q. Lan, *Adv. Energy Mater.*, 2016, **6**, 1600116.
48. J. Xie, H. Zhang, S. Li, R. Wang, X. Sun, M. Zhou, J. Zhou, X. W. D. Lou and Y. Xie, *Adv. Mater.*, 2013, **25**, 5807-5813.
49. D. Tuschel, *Spectroscopy*, 2015, **30**, 14-29.
50. Z. H. Ni, T. Yu, Y. H. Lu, Y. Y. Wang, Y. P. Feng and Z. X. Shen, *ACS Nano*, 2008, **2**, 2301-2305.
51. W. Qiu, X.-Y. Xie, J. Qiu, W.-H. Fang, R. Liang, X. Ren, X. Ji, G. Cui, A. M. Asiri, G. Cui, B. Tang and X. Sun, *Nat. Commun.*, 2018, **9**, 3485.
52. W. Xiong, Z. Guo, S. Zhao, Q. Wang, Q. Xu and X. Wang, *J. Mater. Chem. A*, 2019, **7**, 19977-19983.
53. G. Kresse and J. Hafner, *Physical Review B*, 1993, **47**, 558-561.
54. G. Kresse and J. Furthmüller, *Comput. Mater. Sci.*, 1996, **6**, 15-50.
55. G. Kresse and J. Furthmüller, *Physical Review B*, 1996, **54**, 11169-11186.
56. J. P. Perdew, K. Burke and M. Ernzerhof, *Phys. Rev. Lett.*, 1996, **77**, 3865-3868.
57. G. Kresse and D. Joubert, *Physical Review B*, 1999, **59**, 1758-1775.
58. V. Wang, N. Xu, J. C. Liu, G. Tang and W.-T. Geng, *Journal*, 2019.
59. E. Skúlason, T. Bligaard, S. Gudmundsdóttir, F. Studt, J. Rossmeisl, F. Abild-Pedersen, T. Vegge, H. Jónsson and J. K. Nørskov, *PCCP*, 2012, **14**, 1235-1245.
60. U. Huniar, R. Ahlrichs and D. Coucouvanis, *J. Am. Chem. Soc.*, 2004, **126**, 2588-2601.

View Article Online
DOI: 10.1039/D0TA03622F

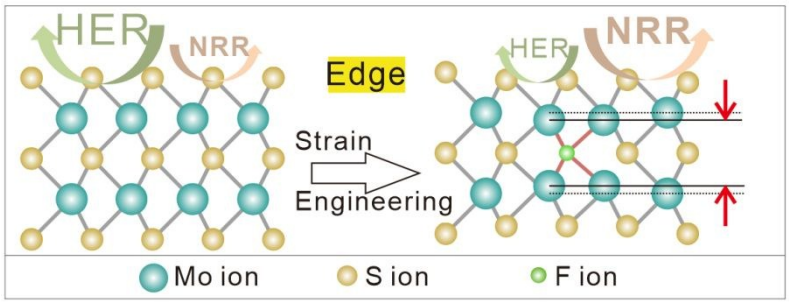

Interlayer space of MoS_2 was compressed by the substituted F ions for the purpose of rationally boosting the NRR activity and selectivity.